ELSEVIER

J. Non-Newtonian Fluid Mech., 69 (1997) 221–237

Journal of Non-Newtonian Fluid Mechanics

Digital particle image velocimetry in flows with nearly closed pathlines: the viscoelastic Taylor–Couette instability

Brandon Max Baumert [a,c], Dorian Liepmann [b], Susan J. Muller [a,c,*]

[a] *Departments of Chemical Engineering, University of California, Berkeley, CA, USA*
[b] *Department of Mechanical Engineering, University of California, Berkeley, CA, USA*
[c] *Center for Advanced Materials, Lawrence Berkeley National Laboratory, Berkeley, CA 94720, USA*

Received 1 July 1996; revised 24 October 1996

Abstract

We describe a novel technique for applying digital particle image velocimetry (DPIV) in steady or slowly varying flows with nearly closed pathlines in which the flow of interest is small relative to the primary flow and the primary flow is normal to the plane of illumination. Despite the fact that in-plane particle displacements are negligible during video-rate image capture, DPIV can be used by implementing extremely low levels of seeding and using long 'exposure' times. An 'exposure' for subsequent DPIV processing corresponds to the image formed by taking the minimum of each pixel position from each of the frames captured during the exposure time. Here, we have used a grey scale in which a pixel value of zero corresponds to white so a bright particle that appears in any of the frames captured during the exposure time will appear in the composite exposure. Preliminary results for a viscoelastic fluid in Taylor–Couette flow (flow between concentric rotating cylinders) are shown. As long as the cylinders are adequately aligned, there is no difficulty in resolving the main features of the secondary flow. Secondary flows four to six orders of magnitude weaker than the base flow can be resolved by this method in the present experiment. This technique would be equally successful in other flows such as flow between rotating parallel disks or between a cone and plate, both of which are important for rheological characterization of fluids. Through the use of co-rotation of fixtures, this technique could also be extended to higher temporal resolution and higher secondary velocities relative to the base flow. © 1997 Elsevier Science B.V.

Keywords: Viscoelastic instability; Secondary flow visualization; Taylor–Couette; Boger fluids

1. Introduction

Particle image velocimetry (PIV) is a non-invasive technique for quantitative, highly time resolved velocity measurements of whole flow fields. In a standard, two-dimensional system,

* Corresponding author.

PII S0377-0257(96)01538-8

illumination of the flow field is provided by a narrow sheet of light. The flow is seeded with tracer particles, and images of the particles are recorded by a camera placed at 90° to the light sheet. The local fluid velocity is determined from images of the location of the particles at two or more times. At high data densities, secondary quantities like the local rate of strain and vorticity may be computed from a spatial differentiation of the velocity fields. Issues related to particle size, seeding density, illumination, image recording, and image interrogation have been reviewed recently by Adrian and Buchhave [1,2]. These authors also discuss accuracy and resolution issues, and provide references to applications of PIV including turbulent channel flows, jets impinging on walls, measurement in an engine model, and evolving vortex rings.

Willert and Gharib [3] described digital particle image velocimetry (DPIV), the extension of PIV techniques to a video-based system in which images are digitally recorded and processed. These authors use sequential images of single-exposed particles and describe the numerical implementation of an FFT-based local spatial cross-correlation (applied to small interrogation regions within the images) to process the images and yield displacement data without directional ambiguity. By using a Gaussian curve-fit to determine the maximum of the highest cross-correlation peak, they are able to obtain sub-pixel accuracy. While the low spatial resolution of CCD arrays relative to photographic film and the low speed at which video frames can be acquired limit the use of DPIV in some situations, it is ideally suited to low speed, slowly varying flows.

A number of authors have suggested schemes for extending PIV and DPIV to three-dimensional flows and this remains an active area of research [4–8]. In most situations, however, resolving an extremely weak velocity component remains difficult. Here, we present a scheme for resolving certain types of secondary flows that are 10^4–10^6 times weaker than the primary flow. The flow must be axisymmetric and have nearly closed pathlines so that if the illumination sheet is normal to the primary flow, an individual particle will undergo only a small displacement between passages through the plane of illumination. By using extremely sparse seeding levels and extremely long 'exposures', composite images are formed which can be processed via standard DPIV algorithms. The long exposure times also require, however, that the flow be steady or very slowly evolving.

These criteria are ideally met by viscoelastic Taylor–Couette flow. Above a critical value of the elasticity, as measured by a Deborah number De (given by the product of a fluid relaxation time λ and a characteristic shear rate $\dot{\gamma}$), the purely azimuthal base flow present when the inner cylinder is rotated is replaced by a very slowly evolving vortex flow. The critical conditions and mechanism of this instability have been studied and discussed in detail by a number of authors [9–14]. Here, we extend earlier flow visualization studies through the use of DPIV techniques to determine quantitatively the evolving secondary velocity and vorticity fields. The technique reveals the rich structure of the evolving disturbance flow. The technique is also expected to work well in a range of other slowly varying, nearly closed pathline flows.

2. Experimental methods

2.1. Viscoelastic fluid preparation and characterization

The viscoelastic fluid used was a dilute solution of high molecular weight polymer in a high viscosity, Newtonian solvent. The solution contained 1000 ppm of polyisobutylene (approximate

molecular weight $4.2–5.2 \times 10^6$ g mol^{-1}) dissolved in oligomeric polybutene (Exxon Parapol 450). This solution falls into the class of fluids referred to as 'Boger' fluids; its shear viscosity η and first normal stress coefficient Ψ_1 are both independent of shear rate over the range of shear rates accessed in the present experiments. At the temperature of the Taylor-Couete experiments, the solution viscosity η is 3.0 poise, the solvent contribution to the viscosity η_s is 2.6 poise, and the first normal stress coefficient Ψ_1 is 0.017 dyne s^2 cm^{-2}. Using the Oldroyd-B constitutive equation to define a relaxation time, λ, based on the steady shear data yields $\lambda = \Psi_1/2(\eta - \eta_s) = 0.021$ s. This fluid is the same as one of those used in our earlier flow visualization studies of the viscoelastic Taylor–Couette instability, and the details of its preparation and rheological characterization are described therein [13].

2.2. Apparatus and illumination

The Taylor–Couette cell, consisting of two concentric cylinders as shown schematically in Fig. 1, has been described in detail elsewhere [13]. The inner cylinder is anodized aluminum with an outer radius of $R_1 = 6.946 \pm 0.001$ cm and the precision bore of the glass outer cylinder has a radius $R_2 = 7.615 \pm 0.003$ cm. The gap-width is thus $d = R_2 - R_1 = 0.669$ cm. The inner cylinder is immersed to a depth $L = 39.5$ cm or 59 gap-widths. The bottom of the cell rotates

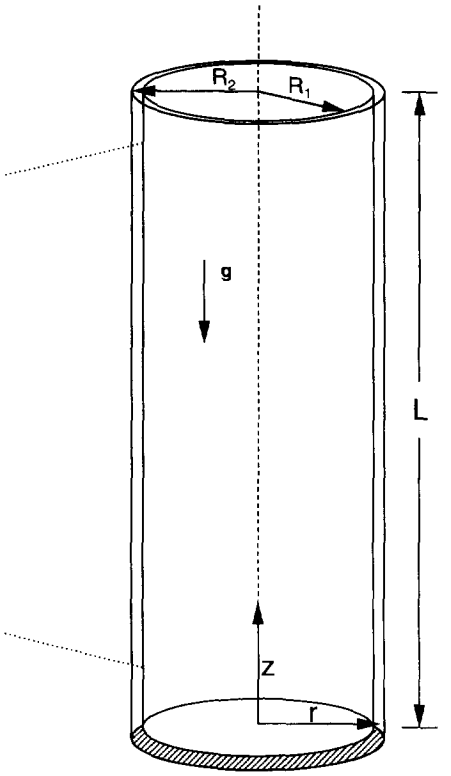

Fig. 1. Taylor–Couette flow cell and orientation of the illuminated gap cross-section. Drawn to scale.

with the outer cylinder and a free surface exists at the top of the cell. A pair of microstepping motors permits smooth, independent rotation of the cylinders; in the present experiments only the inner cylinder was rotated. The outer cylinder is surrounded by a Plexiglas shell containing a refractive index matching and temperature stabilizing mineral oil. Temperatures in the oil bath and inside the oil-filled inner cylinder were maintained at 24 ± 1°C. In each experiment, cylinder rotation was linearly ramped from rest to the final velocity over a period of a few seconds. This acceleration of the cylinder from rest to its final velocity occurred over a time that was consistently several orders of magnitude shorter than the time required for any secondary flows to develop. A number of experiments were performed with considerably slower velocity ramps or with velocity ramps that included a series of plateaus. The sequence of flow states, and the final flow state, was not found to be sensitive to the nature of the velocity ramp for the range examined.

A sheet of laser light 1.5 mm thick, 8 cm in height and coplanar with the cylinder axes was produced using a Coherent Innova 70-2 Argon Ion laser and a non-Gaussian sheet generating lens (Lasiris, Inc.). The seeding was dust and small particles which were present in the viscoelastic fluids used, i.e. no special seed was added. The particle size was estimated to be on the order of a few micrometers.

2.3. Image capture and composite exposure

Images of the gap were obtained using a monochrome CCD video camera (Cohu 4910). Because the onset and evolution of the secondary vortex flow is exceedingly slow, typical experiments lasted 2–8 h and video-rate (30 frames s^{-1}) capture was deemed unnecessary (due to the slow temporal changes) and impractical (due to the huge storage requirements). Instead, the Cohu camera was operated in an on-chip integration mode in which it collected light for a specified period and then output a frame to a frame grabber (Scion LG-3) installed in a Macintosh Quadra 840AV laboratory computer. By averaging for several seconds on-chip, 90% of the video signal or more can be captured and stored continuously to the hard disk for many hours. A 4.5 s on-chip integration time (with an additional 0.5 s to write to disk) was typically used to capture a 256×640 pixel region of interest at a 5 s refresh period.

These 4.5 s frames were subsequently used to produce composite images for DPIV processing which represented longer exposure times. Using a grey scale in which zero represents white and 255 represents black, the bright, reflective seed particles correspond to local minima in each digital image. By taking the minimum of each pixel position for a series of sequential frames, a particle appearing in any of the frames captured during the exposure time appears in the composite image. If the particle undergoes no displacement between frames, it appears as a single particle; if a particle is displaced between subsequent frames and is captured in more than one frame it will appear more than once in the composite image. Note that composite exposures could also be formed from frames captured at video rate if the evolution of the flow warranted better temporal resolution.

In the present case, five sequential frames (each corresponding to a 4.5 s on-chip exposure) were used to create a composite image corresponding to a 25 s exposure or approximately 30 revolutions of the inner cylinder. During this period, a particle at the inner cylinder passes through the illuminated plane 30 times. While a particle at the fixed outer cylinder will never

rotate through the plane, n rotations of the inner cylinder will cause all particles further than $1/n$-th the gap width away from the outer cylinder to be imaged at least once. In a single 4.5 s exposure, the density of Imaged particles near the outer cylinder was quite low in that seeding was extremely sparse. However, since a large number of frames are combined as described to a single 25 s exposure, every seed particle present in the cell at $R_1 < r < R_2 - 1/30\ (R_2 - R_1)$ and in the axially captured range will appear in each image used for DPIV processing. This provides a seeding density of approximately 25 particles in the 64×64 pixel sampling window, with particles typically occupying a single pixel.

2.4. DPIV processing

The images were processed using the algorithms described in Willert and Gharib (1991). Two sequential 25 s exposure images were processed for each data set. The sampling window was 64×64 pixels, and the step size was 32 pixels, providing 50% of overlap between adjacent interrogation regions. Spurious vectors were removed by applying a local median filter that considers both the magnitude and direction of a velocity measurement in relation to the eight neighboring points [15,16]. No more than 5% of the total vectors were re-interpolated in the post-processing procedure. The resulting vector field was then averaged with the next four vector fields produced from the temporally adjacent 25 s exposures; as a result each vector field represented an average over 125 s. Shorter exposures were used when maximum velocities would have resulted in displacements between composite images of more than a quarter of an interrogation region. Vorticity distributions were computed from the velocity vector fields using a two-dimensional, second order finite difference scheme that employs the eight neighboring data points.

3. Results

A sequence of images showing the seed distribution and streak patterns in the illuminated gap between the concentric cylinders is shown in Fig. 2. The shear rate $\dot{\gamma}$ Reynolds and Deborah numbers are defined as

$$\dot{\gamma} = \frac{|\Omega_2 - \Omega_1|R_1}{(R_2 - R_1)}, \qquad Re = \frac{|\Omega_2 - \Omega_1|R_1(R_2 - R_1)}{(\eta/\rho)}, \quad \text{and} \quad De = \dot{\gamma}\lambda,$$

where Ω_1 and Ω_2 are the inner and outer cylinder angular velocities respectively, ρ is the solution density, and η is the solution viscosity. In these and all subsequent images, the outer cylinder is at the top of each image, the inner cylinder at the bottom, and the axial coordinate z increasesfrom left to right. Here, the images from the CCD camera, acquired at a 5 s interval, were post-processed by taking the minimum of each pixel position for a set of 25 sequential images. This produced images with 125 s exposure times and streak patterns which indicate the broad features of the flow qualitatively. The conditions shown in Fig. 2, $De = 1.78$, $Re = 10.8$, correspond to the apparent critical condition for the onset of the viscoelastic instability; i.e., these are the lowest values of De and Re for which a flow transition was observed in this fluid. A purely azimuthal shearing flow is quickly established as the inner cylinder is ramped from rest

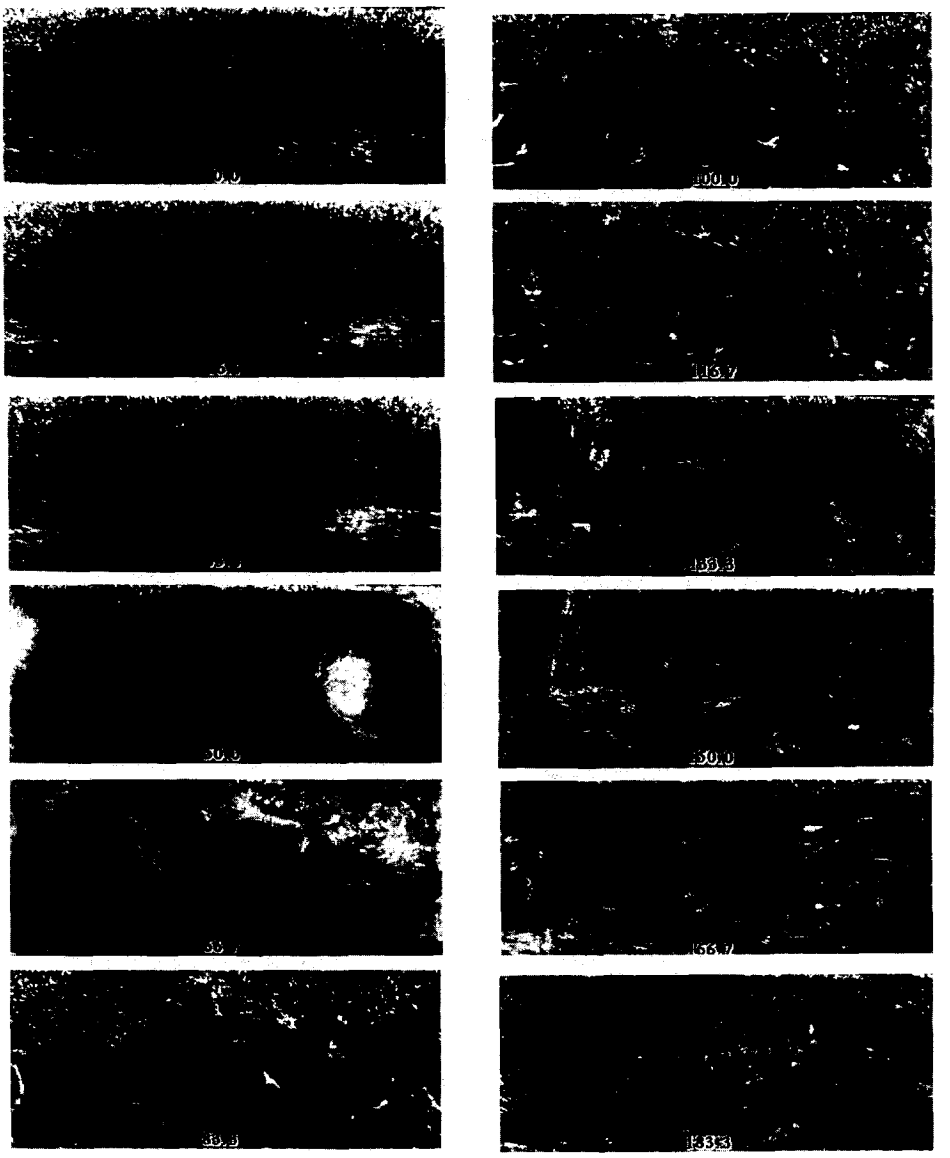

Fig. 2. Seeding distribution and streak patterns at $\dot{\gamma} = 84.8\ s^{-1}$, $De = 1.78$, $Re = 10.8$. Images represent 125 s exposures and are shown at an interval of 1000 s. The images are labeled with the time in minutes since the beginning of shear. The inner cylinder is at the bottom of each image, the outer cylinder is at the top and height in the flow cell increases to the right.

to its final velocity. This base flow, and the absence of any apparent secondary flow, is evident in the first three frames of Fig. 2. After approximately 45 min, counter-rotating Taylor-type vortices form, filling the gap between the cylinders. Following several minutes of relatively strong secondary flow, very irregular vortices of higher axial wavenumber form and are

particularly apparent 83 min into the experiment. These distorted vortices are eventually replaced by stationary counter-rotating vortices that are similar in strength and wavenumber to those which initially formed. The stationary vortices persist until the experiment is stopped after nearly 200 min of shearing.

Fig. 3 shows a source image pair for DPIV processing from the same experiment as in Fig. 2. Also shown is the resulting velocity vector map produced using the processing steps outlined in Section 2. In comparing the images in Figs. 2 and 3, note that there is a factor of five difference in exposure time; the DPIV source images represent 25 s exposures and so appear less densely seeded than those in Fig. 2. The resulting vector map from this single pair of images, taken at a point in the experiment where the secondary flow is near its maximum strength, clearly shows the vortex structure. In addition, while the azimuthal velocity of the inner cylinder is 56.7 cm s^{-1}, our processing allows us to resolve axial and radial velocities that are on the order of 5×10^{-4} cm s^{-1}.

The sequence of velocity vector maps corresponding to Fig. 2 is shown in Fig. 4. Note that the effective exposure time is identical in the two figures since five sequential 25 s exposure-based velocity fields were temporally averaged to produce each field in Fig. 4. While the imaging and processing conditions used here clearly resolve the strong, gap-spanning vortices present at 50

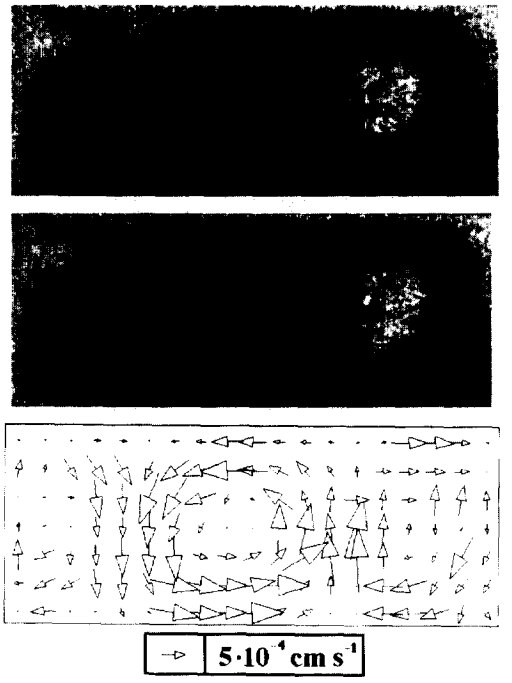

Fig. 3. Source image pair and resulting (r, z)-velocity vector map produced using digital particle image velocimetry. Orientation is as in Fig. 2. The inner cylinder is rotating at 1.3 rps, $\dot{\gamma} = 84.8$ s^{-1}, $De = 1.78$, $Re = 10.8$. The first source image is 52.1 min after shear initiation (near the peak of vortex velocity). Source images are exposed for 25 s and are separated by 25 s. An axial or radial velocity corresponding to the length of the vector in the legend box is 5×10^{-4} cm s^{-1}. The azimuthal velocity at the inner cylinder is 56.7 cm s^{-1}.

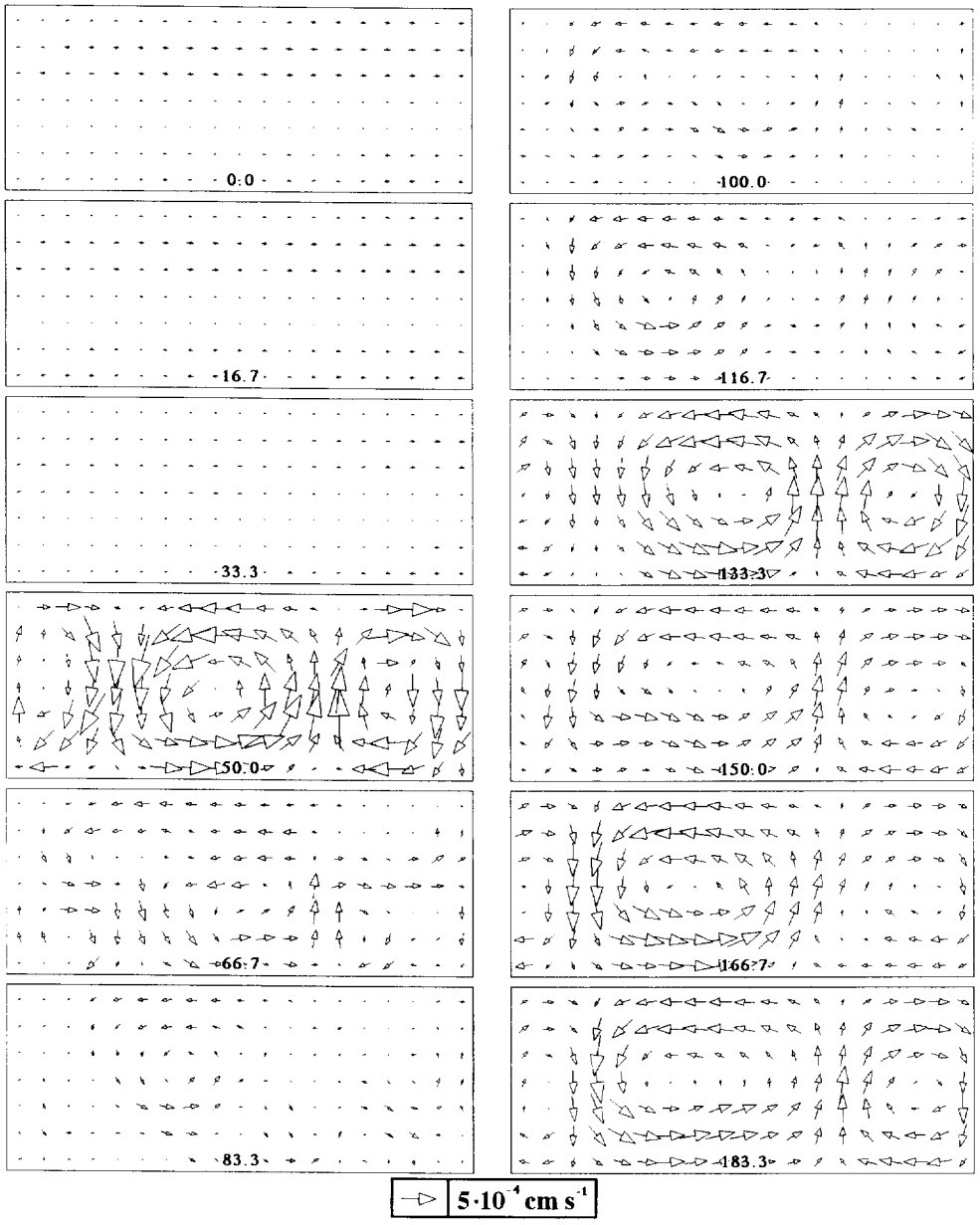

Fig. 4. Overview of the evolution of the (r, z)-velocity field at $\dot{\gamma} = 84.8\ s^{-1}$, $De = 1.78$, $Re = 10.8$. Time in minutes since initiation of shear is indicated. Velocity fields are presented at a 1000 s interval and are averages over 125 s.

min and at times greater than 116 min, the higher wavenumber, distorted vortices present at intermediate times are less well captured. This is not surprising given the relatively large interrogation region used.

In addition to quantifying the elastic secondary flow as described above, the first three frames of Fig. 4 reveal a very weak flow upward near the outer cylinder and downward near the inner cylinder. This weak flow (which is also evident in experiments with the viscous Newtonian solvent which shows no elasticity and no counter-rotating vortices at these Re) appears consistent with a very small amount of natural convection. While constant temperature mineral oil was recirculated both through the hollow inner aluminum cylinder and outside the glass outer cylinder to keep the temperature constant, the thick glass of the outer cylinder acted essentially as a thermal insulator. Based on the fluid properties and the shear rate corresponding to Fig. 4, we estimate the maximum temperature rise caused by viscous heating to be approximately 0.25°C with the maximum temperature occurring at the outer cylinder wall.

By processing all of the data from the experiment in Fig. 2 at 125 s intervals, the temporal evolution of the flow can be mapped out in much greater detail than that indicated in Fig. 4. As a measure of the strength of the secondary flow, Fig. 5 shows the magnitude of the average radial velocity $|\bar{v}_r|$ as a function of time following initiation of inner cylinder rotation. Here, $|\bar{v}_r|$ is defined as

$$|\bar{v}_r| = \frac{1}{(R_2 - R_1)(z_2 - z_1)} \int_{z_1}^{z_2} \int_{R_1}^{R_2} |v_r| \, dr \, dz.$$

The extremely long time between initiation of shear flow and the onset of the secondary flow, as well as the extremely slow evolution of the secondary flow, are apparent in both Figs. 2 and 5. The several orders of magnitude difference between the onset or evolution times and the relaxation time of the viscoelastic fluid remains unexplained. Not revealed in Fig. 2 but made explicit in Fig. 5 are additional features of this flow. First, the strength of the vortex flow undergoes a number of clearly defined oscillations before settling down to a steady vortex flow. These oscillations become damped but persist for nearly the entire 200 min of the run. In addition, at all intermediated times when the distorted vortices are present, there is still a resolvable secondary flow. As noted above, however, the relatively large size of our interrogation

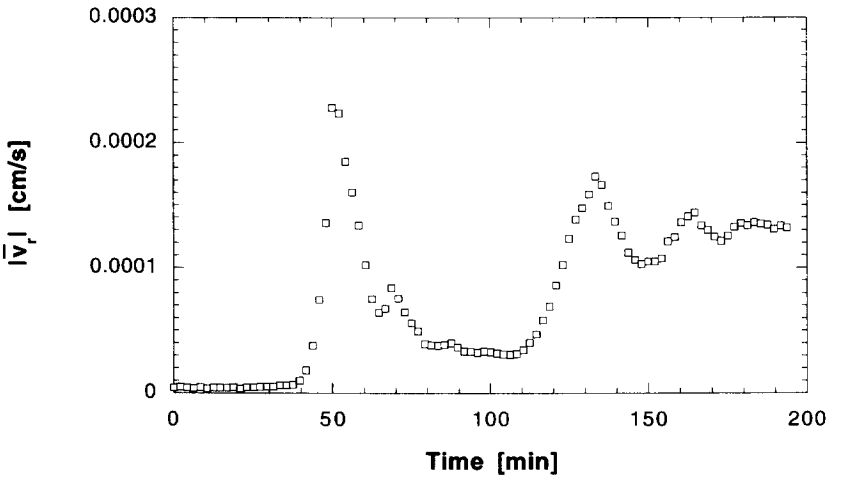

Fig. 5. History of the average radial velocity magnitude at $\dot{\gamma} = 84.8\ s^{-1}$, $De = 1.78$, $Re = 10.8$ over 125 s periods.

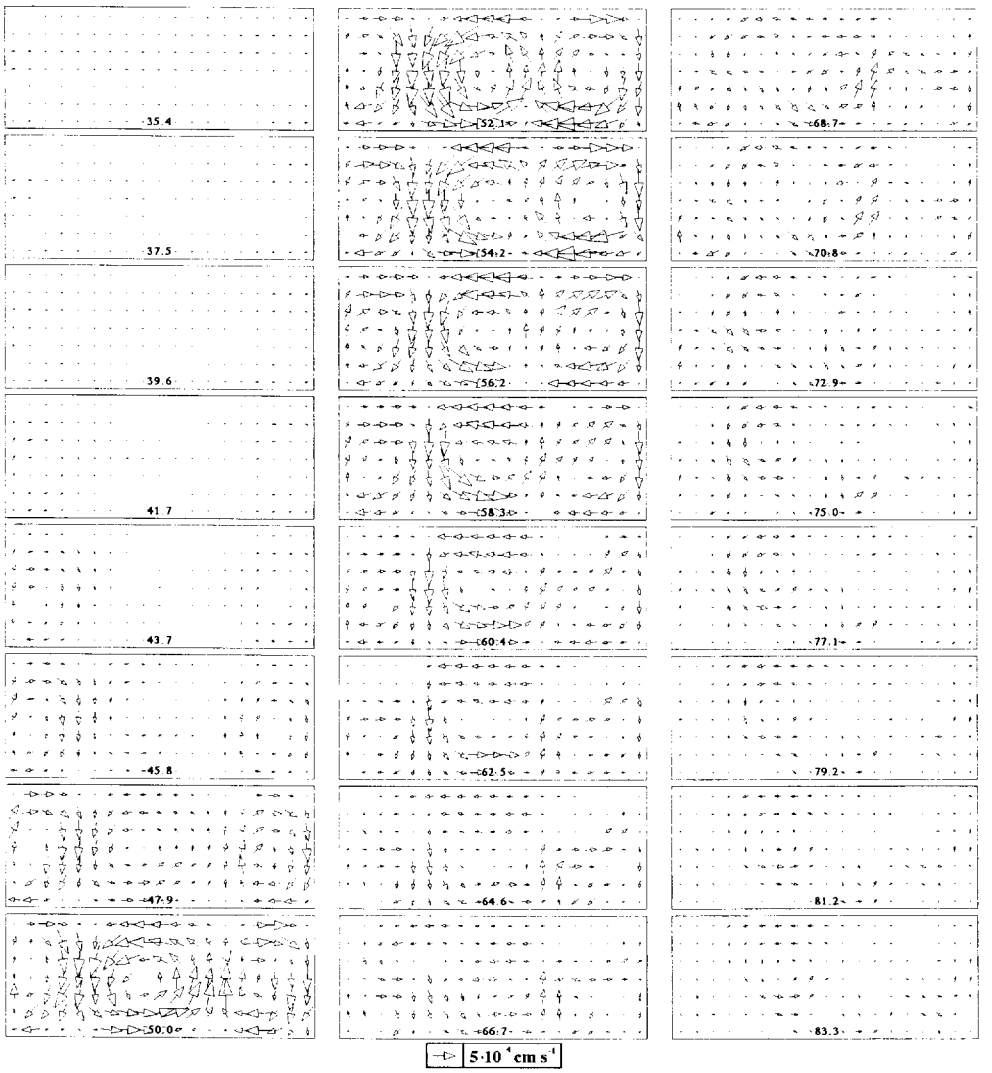

Fig. 6. Evolution of the (r, z)-velocity field at $\dot{\gamma} = 84.8\ s^{-1}$, $De = 1.78$, $Re = 10.8$ spanning the first peak of vortex strength. Time in minutes since initiation of shear is indicated. The first field is at 35.4 min, the interval between fields is 125 s and fields are averages over 125 s.

region does not adequately capture the fine structure of the higher wavenumber vortices and so the true magnitude of the average radial velocity is probably somewhat higher than Fig. 5 indicates.

The temporal evolution of the velocity field during the time intervals spanning the two highest peaks in Fig. 5 is shown in Figs. 6 and 7. Once the initial vortices form, they appear to retain their identity; the vortices visible in the lower left hand frame of Fig. 6 have the same axial position and sense of rotation throughout the experiment and are identifiable even when the secondary flow is relatively weak and disordered (as in the third column of Fig. 6). The same

vortices are also identifiable in Fig. 7, where they have strengthened and undergone some shifting in their axial wavenumbers.

The vorticity distribution was computed using a six point difference for each derivative, e.g.

$$\left(\frac{\partial v}{\partial y}\right)_{ij} = \frac{(v_{i+1,j+1} + 2v_{i,j+1} + v_{i-1,j+1}) - (v_{i+1,j-1} + 2v_{i,j-1} + v_{i-1,j-1})}{8\delta y}.$$

Fig. 8 shows the evolution of the vorticity field from the inception of shearing through the end of the experiment. The rapid increase in vorticity at about 45 min is evident, as are the subsequent oscillations in vorticity. Spatial resolution issues, especially in the radial direction, suggest that the calculated vorticity values are probably somewhat lower than the actual values.

The evolution of the secondary flow is similar at a somewhat higher *De* and *Re*. Fig. 9 shows a series of velocity fields for an experiment at a slightly higher shear rate than the previous one, corresponding to $De = 2.74$ and $Re = 16.7$. (Note that since the fluid material properties are independent of shear rate, the ratio of *De* to *Re* is fixed for this fluid at $De/Re = 0.16$). The velocity fields again indicate an initial, purely azimuthal flow followed by strong, stationary counter-rotating vortices which decrease and then increase in strength. Here, the azimuthal velocity at the inner cylinder is 87.3 cm s^{-1}, and radial and axial velocities on the order of 2×10^{-4} cm s^{-1} are resolvable. In periods of the experiment with high maximum velocities, a 10 s effective exposure time was used instead of the default 25 s. The entire progression of flow states occurs over a shorter time at this higher shear rate, but the final state again appears to be steady Taylor-like vortices which span the gap between the cylinders. The difference in axial wavenumbers between these two experiments is comparable with the variations that occurred for multiple runs at the same conditions.

The magnitude of the average radial velocity for this run, computed as for Fig. 5, is shown in Fig. 10. Shown in the inset is the first 25 min of the same run processed using a shorter 50 s average to better resolve the initial maximum in average radial velocity near 14 min, which is

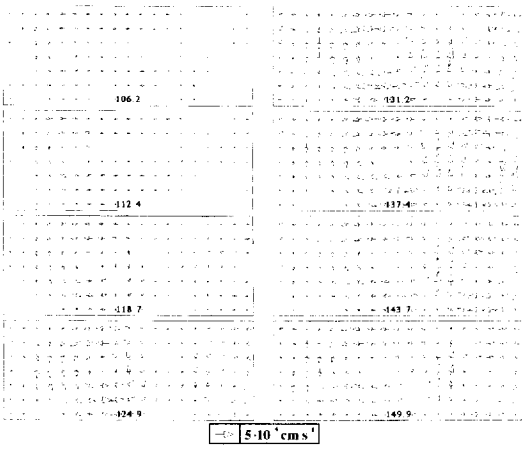

Fig. 7. Evolution of the (r, z)-velocity field at $\dot{\gamma} = 84.8$ s^{-1}, $De = 1.78$, $Re = 10.8$ spanning the second major peak of vortex strength. Time in minutes since initiation of shear is indicated. The first field is at 106.2 min, the interval between fields is 375 s and fields are averages over 125 s.

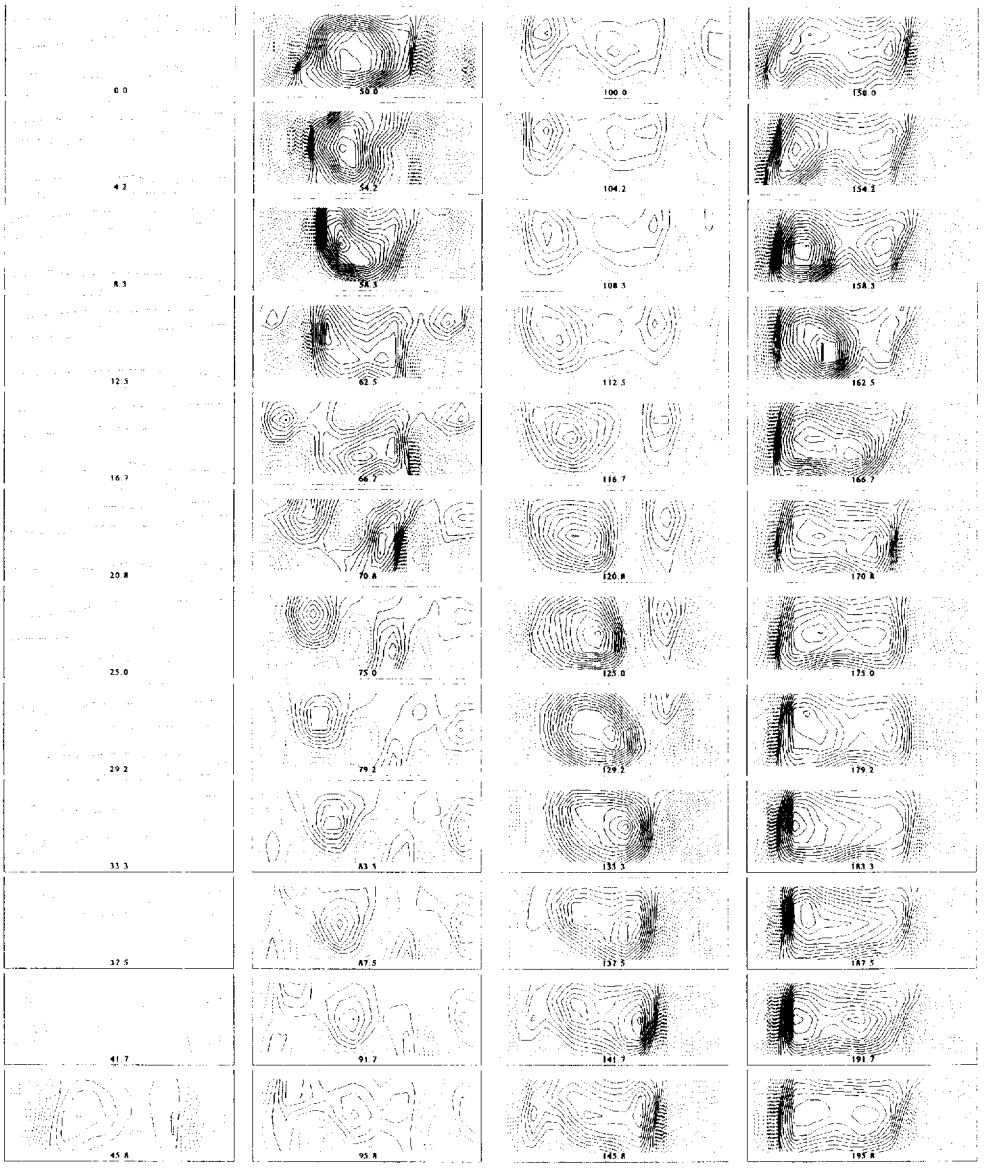

Fig. 8. Vorticity evolution at $\dot{\gamma} = 84.8\ s^{-1}$, $De = 1.78$, $Re = 10.8$. Constant vorticity contour maps are presented at a 250 s interval and are averages over 125 s. Positive vorticity is represented by solid lines and negative vorticity by dashed lines. Vorticity at adjacent contours differs by $4 \times 10^{-4}\ s^{-1}$.

followed by a second, lower peak and a period of very weak vortex motion. Fig. 10 displays, the same features as Fig. 5: a long onset time (relative to the fluid relaxation time) following initiation of shear, a long time to reach a steady value of the average radial velocity, and large initial oscillations in the strength of the secondary flow. In contrast to the lower rate run,

however, the final average radial velocity is higher than the initial maximum. The temporal evolution of the vorticity distribution for the first 39 min of the experiment is shown in Fig. 11. Again, we note that the vortices that initially form at approximately 13 min retain their axial location and sense of rotation and are identifiable after the second maximum in $|\bar{v}_r|$.

4. Discussion

In this study the lowest rate viscoelastic transition in Taylor–Couette flow has been examined using a novel implementation of DPIV that is well suited to this slowly evolving flow with nearly closed pathlines. We have presented maps of velocity and vorticity fields near the onset of the viscoelastic instability. In addition to providing benchmarks for numerical simulations of this flow, these data reveal for the first time the complexity of the temporal progression of the vortex strength. The DPIV was performed at a spatial resolution sufficient to represent quantitatively

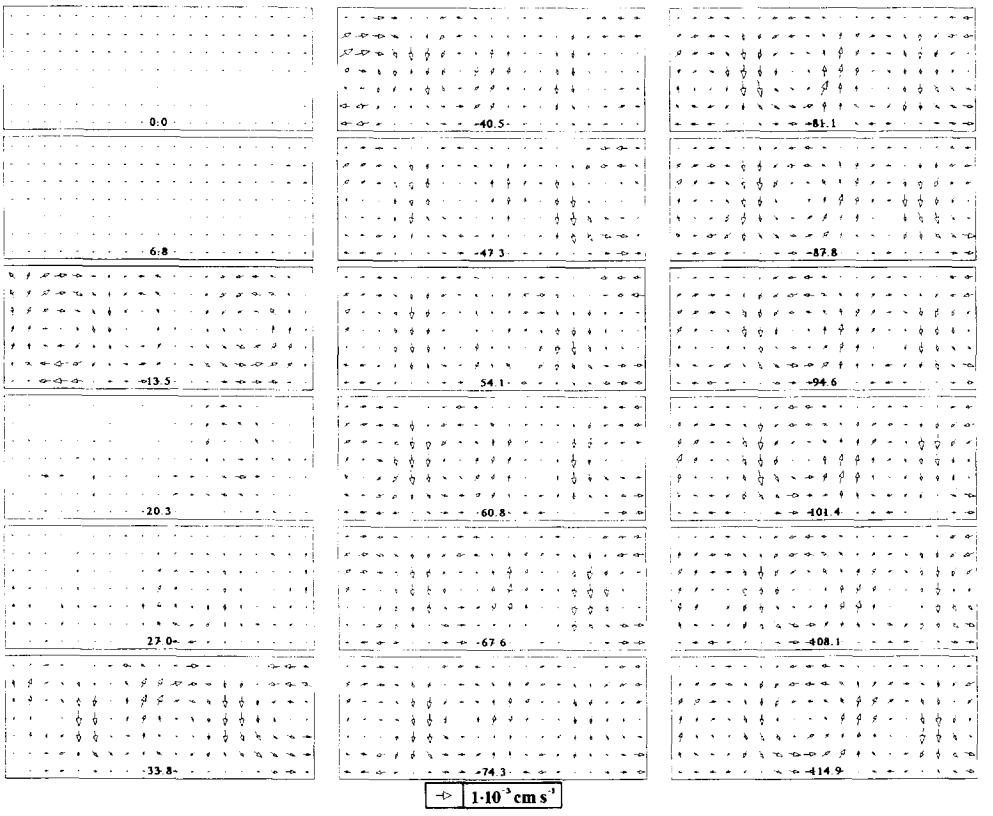

Fig. 9. Evolution of the (r, z)-velocity field at $\dot{\gamma} = 130.5\ s^{-1}$, $De = 2.74$. $Re = 16.7$. Time in minutes since initiation of shear is indicated. Velolcity fields are presented at a 405 s interval and are averages over 100 s. An axial or radial velocity corresponding to the length of the vector in the legend box is 1×10^{-3} cm s^{-1}. The azimuthal velocity at the inner cylinder is 87.3 cm s^{-1}.

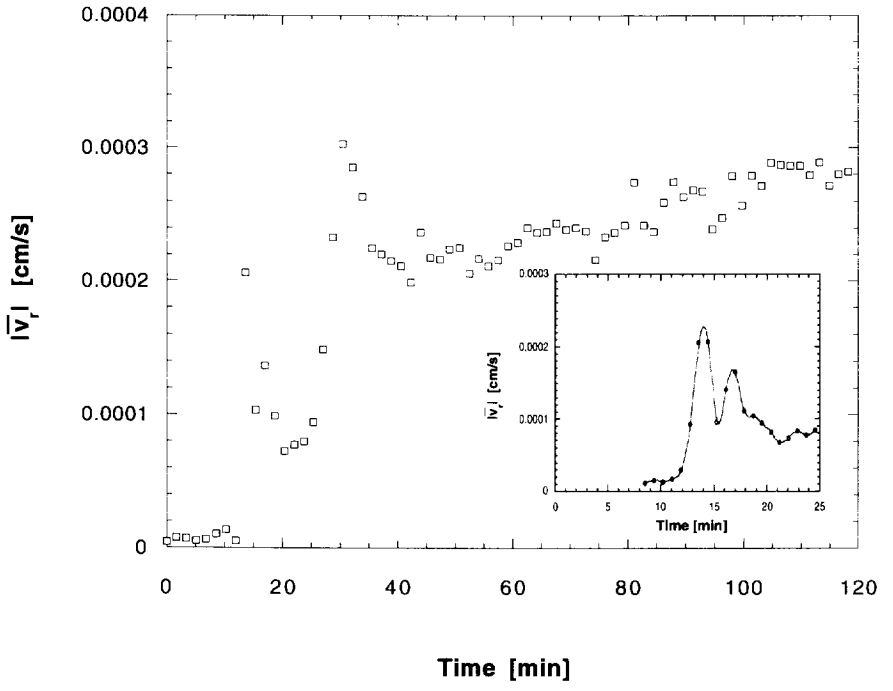

Fig. 10. History of the average radial velocity magnitude at $\dot{\gamma} = 130.5\ s^{-1}$, $De = 2.74$, $Re = 16.7$. Averages are over 100 s in the main plot and over 50 s in the inset plot.

the gap-spanning vortices that are the characteristic secondary flow in the experiments. However, a comparison with streak patterns suggests that better spatial resolution—achievable through higher levels of neutrally buoyant seeding—is necessary to faithfully capture the smaller, higher wavenumber vortices which exist briefly after the first velocity peak. Figs. 5 and 10 represent the only experiments in which data have been collected and processed such that the damped oscillations and the finer time scale structure is quantified. However, earlier extensive flow visualization experiments using mica alignment (rather than DPIV) in the gap cross section [13,14] demonstrated that the temporal sequence of transitions, the time to onset of the strong vortices, and the eventual plateau in vortex strength are highly reproducible.

In systems with a very minor velocity component in the imaged plane, the lower limit on measurable in-plane velocities is set only by the rate of buoyant drift of the seeding particles. However, when a fixture must be rotated several times in order to allow most of the particles to pass through the imaging plane at least once, an upper velocity limit exists. If we wish to investigate the inner 75% of the gap in a Couette cell, the inner cylinder must rotate four times. And if we require four independent velocity vectors across the gap and particle displacements between image pairs less than 25% of an interrogation region, we are limited to motions of less than 1/64 of a gap width per cylinder rotation (2.4×10^{-4} of the base flow in our geometry.) The maximum velocities in the flows examined here were well below this limit.

In systems with a single rotational axis of symmetry (circular Couette, cone and plate, rotating parallel disks, and lid driven flows in a circular cylinder) the temporal resolution of the

technique can be increased by co-rotating the fixtures. The exposure period of each analyzed image can then be matched to the period of rotation of the slower fixture. An advantage of this scheme is the elimination of particle drop out near a fixed surface. Temporal resolution is limited only by the chosen rate of co-rotation. With the co-rotation rate enough in excess of the difference of the rotation rates, particle imaging can be performed frequently enough that the restriction to flows having nearly closed pathlines is relaxed. Note that a centrifugal body force increases with increasing co-rotation, however, potentially modifying the behavior of the system.

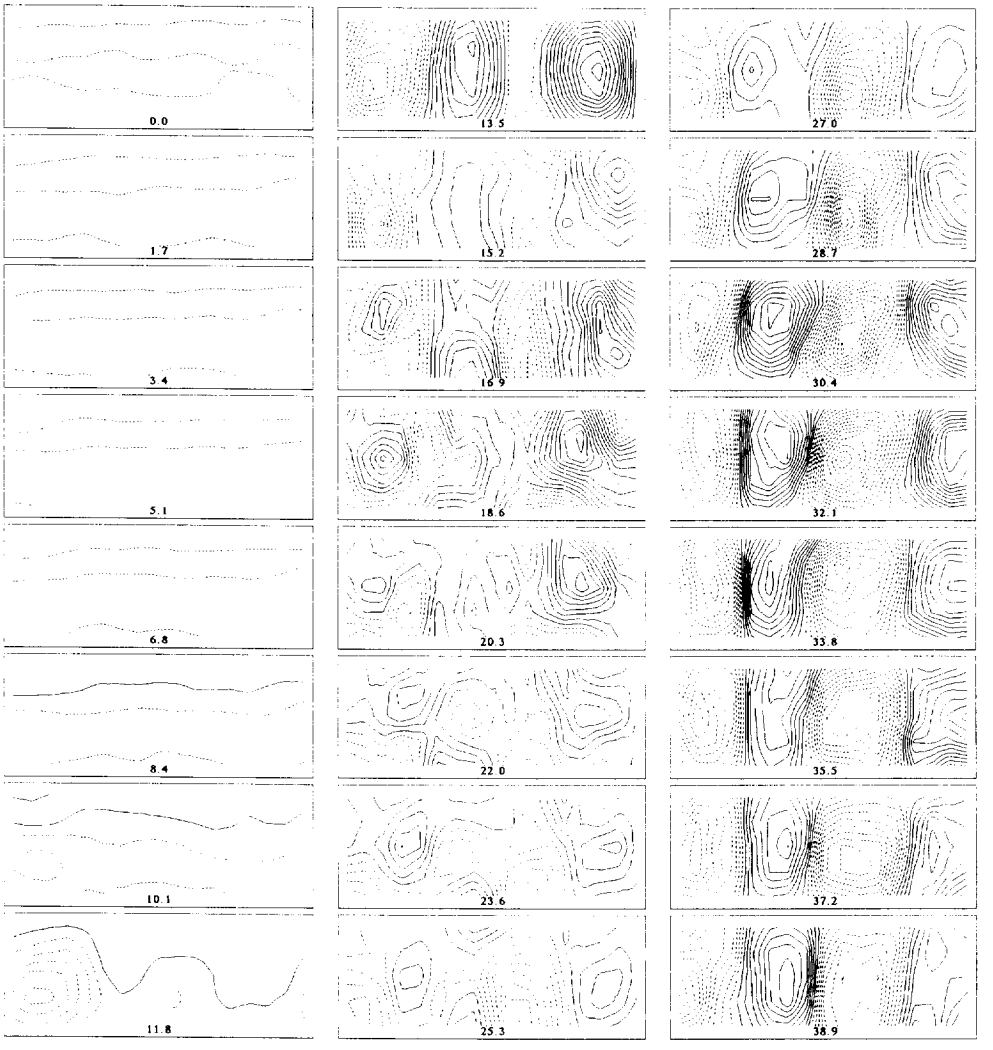

Fig. 11. Vorticity evolution at $\dot{\gamma} = 130.5\ s^{-1}$, $De = 2.74$, $Re = 16.7$ up to the beginning of the apparent long-time plateau. Constant vorticity contour maps are presented at a 101 s interval and are averages over 100 s. Positive vorticity is represented by solid lines and negative vorticity by dashed lines. Vorticity at adjacent contours differs by $9.88 \times 10^{-4}\ s^{-1}$.

For instance, Marcus [17] predicts in Newtonian Taylor–Couette flow with $R_1/R_2 = 0.5$ a change of the critical axial wavenumber from 3.161 with a fixed outer cylinder to 3.000 in a system with $\Omega_1/\Omega_2 = 0.16667$. Imaging under co-rotation also imposes strict requirements on the alignment and axisymmetry of the erstwhile fixed fixture.

In systems not having a single rotational axis of symmetry (eccentric rotational flows, rectangular cavity with a rotating lid, rotating circular cylinder in a rectangular cavity, and a rectangular cavity with a translating lid) co-rotation is not an option. What is obtained from the present DPIV implementation is then not a velocity map, but a measure of the displacement of particles on successive passes through the illuminated plane, analogous to a Poincaré map. Velocities are obtained directly only for axisymmetric flows cells with a single rotational axis of symmetry.

Acknowledgements

This work was supported in part by the Director, Office of Energy Research, Office of Basic Energy Sciences, Materials Science Division of the US Department of Energy under contract number DE-AC03-76SF00098. The authors also wish to acknowledge gifts to support polymer research from the AT&T Foundation. BMB acknowledges support form the National Science Foundation Graduate Research Fellowship Program.

References

[1] R.J. Adrian, Particle-imaging techniques for experimental fluid mechanics, Annu. Rev. Fluid Mech., 23 (1991) 261–304.
[2] P. Buchhave, Particle image velocimetry-status and trends, Exp. Thermal Fluid Sci., 5 (1992) 586–604.
[3] C.E. Willert and M. Gharib, Digital particle image velocimetry, Exp. Fluids, 10 (1991) 181–193.
[4] C. Brucker, Digital-particle-image-velocimetry (DPIV) in a scanning light-sheet: 3D starting flow around a short cylinder, Exp. Fluids, 19 (1995) 255–263.
[5] M. Raffel, M. Gharib, O. Ronneberger and J. Kompenhans, Feasibility study of three-dimensional PIV by correlating images of particles within parallel light sheet planes, Exp. Fluids, 19 (1995) 69–77.
[6] C.E. Willert and M. Gharib, Three-dimensional particle imaging with a single camera, Exp. Fluids, 12 (1992) 353–358.
[7] H. Meng and F. Hussain, Holographic particle velocimetry: a 3D measurement technique for vortex interactions, coherent structures, and turbulence, Fluid Dyn. Res., 8 (1991) 33–52.
[8] A.K. Prasad and R.J. Adrian, Stereoscopic particle image velocimetry applied to liquid flows, Exp. Fluids, 15 (1993) 49–60.
[9] D.W. Beard, M.H. Davies and K. Walters, The stability of elasto-viscous between rotating cylinders, J. Fluid Mech., 24 (1966) 321–334.
[10] R.G. Larson, E.S.G. Shaqfeh and S.J. Muller, A purely elastic instability in Taylor–Couette flow, J. Fluid Mech., 218 (1990) 573–600.
[11] Y.L. Joo and E.S.G. Shaqfeh, The effects of inertia on the viscoelastic Dean and Taylor–Couette flow instabilities with application to coating flows, Phys. Fluids A, 4 (1992) 2415–2431.
[12] R. Sureshkumar, A.N. Beris and M. Avgousti, Non-axisymmetric subcritical bifurcations in viscoelastic Taylor–Couette flow, Proc. R. Soc. Lond. A, 447 (1994) 135–153.
[13] B.M. Baumert and S.J. Muller, Flow visualization of the elastic Taylor-Couette instability in Boger fluids, Rheol. Acta, 34 (1995) 147–159.

[14] B.M. Baumert and S.J. Muller, Flow regimes in model viscoelastic fluids in a circular Couette system with independently roating cylinders, Phys. Fluids, in press (1997).
[15] J. Westerweel, Digital Particle Image Velocimetry-theory and application, PhD Thesis, Technical Universtiy of Delft, 1993.
[16] D. Fabris, Combined experimental and numerical investigations of a vortex ring impinging normally on a wall, PhD Thesis, University of California, Berkeley, 1996.
[17] P.S. Marcus, Simulation of Taylor–Couette flow. Part 1. Numerical methods and comparison with experiment, J. Fluid Mech., 146 (1984) 45–64.